Letter

Higher-order topological insulators in two-dimensional Dirac materials

Yang Xue,[1,*] Hao Huan,[2] Bao Zhao,[2,3] Youhua Luo,[1] Zhenyu Zhang,[4] and Zhongqin Yang[2,†]

[1]*School of Physics, East China University of Science and Technology, Shanghai 200237, China*

[2]*State Key Laboratory of Surface Physics and Key Laboratory of Computational Physical Sciences (MOE) & Department of Physics, Fudan University, Shanghai 200433, China*

[3]*Shandong Key Laboratory of Optical Communication Science and Technology, School of Physics Science and Information Technology, Liaocheng University, Liaocheng 252059, China*

[4]*International Center for Quantum Design of Functional Materials (ICQD), Hefei National Laboratory for Physical Sciences at Microscale, and CAS Center for Excellence in Quantum Information and Quantum Physics, University of Science and Technology of China, Hefei 230026, China*

(Received 5 September 2021; accepted 30 November 2021; published 23 December 2021)

As a novel topological state, a higher-order topological insulator has attracted enormous interest, which in d spatial dimensions has gapless boundary states at (d-n) dimensions (integer n is larger than 1). Until now, merely few two-dimensional (2D) materials have been identified as higher-order topological insulators and their experimental confirmations are still absent. Here we propose a universal strategy of antidot engineering to realize second-order topological insulators (SOTIs) in 2D Dirac materials. Based on symmetry analysis, tight-binding model, and first-principles calculations, we demonstrate SOTIs in antidot-decorated Xene (X=C, Si,and Ge) by displaying its finite bulk quadrupole moment, weak topological edge states, and in-gap topological corner states. An inherent connection is established for the existing various mechanisms of the SOTIs, including quadrupole polarization, filling anomaly, and generalized Su-Schrieffer-Heeger model on a Kekulé lattice. The robustness of topological corner states of the SOTIs against edge perturbations and bulk disorders is explicitly demonstrated, rendering our strategy appealing to experimental realization of topological corner states.

DOI: 10.1103/PhysRevResearch.3.L042044

Introduction. Recently, a new type of topological insulator, the two-dimensional second-order topological insulator (2D SOTI), has been proposed and has attracted considerable attention [1–18]. The 2D SOTI can exhibit 1D gapped edge states and 0D in-gap corner states. However, very few 2D electronic materials have been reported to host SOTIs [9,10,12]. Experimental confirmation of the corner states of an SOTI in electronic systems is still absent [15]. It is therefore of extreme importance to find a generalized and experimentally achievable proposal to produce SOTIs in 2D electronic materials.

Due to their rich and exotic properties, 2D Dirac materials such as Xenes (X = C, Si, and Ge) [19], carbon and boron allotropes [20], and metal-organic frameworks [21], etc. have been widely explored [19–27], and many of them have been synthesized successfully in experiments [19,20,22–24]. In the most typical case, the linear Dirac dispersion can be interpreted coming from a pair of spinless p_z-like orbitals that reside separately on honeycomblike lattices (planar or buckled). This feature can actually be employed to introduce higher-order topology in Dirac materials, which is illustrated in Fig. 1. The pair of spinless p_z-like orbitals above can induce a connected elementary band representation (EBR) [28–32] whose corresponding Wyckoff positions are at the honeycomb lattice sites [29,30]. If we extend the cell to a supercell such as a $\sqrt{3} \times \sqrt{3}$ supercell [Fig. 1(a)], the pristine lattice sites and orbitals on them will not be at the maximal Wyckoff positions [29,30] of the supercells. Thus, the equivalent and repeating p_z-like orbitals will induce a connected composite band representation (CBR) [29,30], corresponding to the folded energy bands [Fig. 1(b)]. As the orbitals mentioned above are all at the nonmaximal Wyckoff positions, the obtained CBR must equal a (direct) sum of some EBRs whose corresponding Wyckoff positions are maximal positions in the supercell. In addition, we can add a perturbation that maintains the symmetry of honeycomblike lattices but expands the primitive cell. The symmetry-preserving perturbation may split the connected CBR into some separated EBRs. If the Fermi level (E_F) resides in the band gap between these EBRs, the introduced perturbation will shift the Wannier function centers (also charge centers) of the pristine honeycomblike system and result in an obstructed atomic limit (OAL) [29,30,33] [Fig. 1(a)], which may give rise to symmetry-protected topological corner states [1,2,13,14]. In Fig. 1(c) and Fig. 1(d), we consider the intersublattice intervalley scattering as an example of symmetry-preserving perturbations that can be characterized as a Kekulé-like hopping texture in real space [Fig. 1(a)] [34]. By tuning the

*xuey@ecust.edu.cn
†zyang@fudan.edu.cn

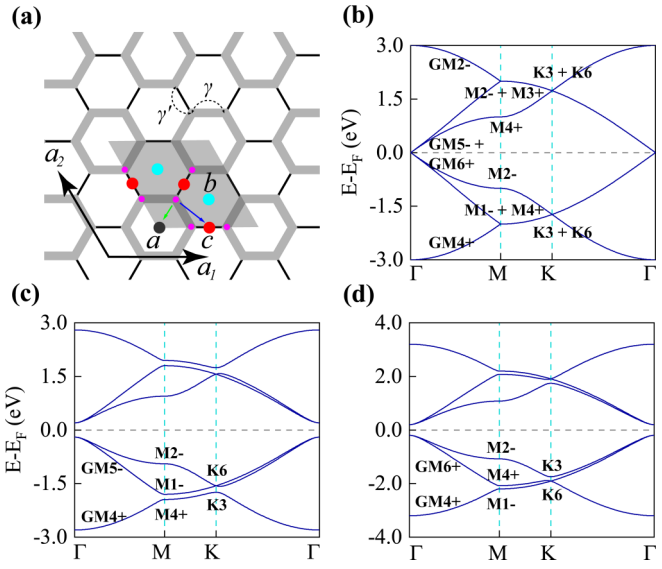

FIG. 1. (a) Lattice structure of a honeycomb lattice with a Kekulé-like hopping texture. Thick and thin bonds represent the intracellular (γ) and intercellular (γ') hopping, respectively. The gray rhombus is the unit cell that is identical to the $\sqrt{3} \times \sqrt{3}$ supercell of the pristine unit cell with six nonequivalent lattice sites (denoted in magenta). The maximal Wyckoff positions in the supercell are indicated in black, red, and cyan blue. The green and blue arrows represent the shift of the Wannier function center of the occupied bands from case (b) to case (c) and case (d), respectively. Energy band structure of a honeycomb lattice with an alternating hopping texture: (b) $\gamma/\gamma' = 1.0$, i.e., graphenelike case; (c) $\gamma/\gamma' = 1.2$, i.e., trivial case; and (d) $\gamma/\gamma' = 0.8$, i.e., nontrivial case. The Wannier function centers of the occupied bands in cases (b), (c), and (d) are at the positions labeled in magenta, black, and red, respectively. The cases (c) and (d) are in two different OALs.

perturbation strength (difference in hopping amplitudes), two different OALs are obtained (for details, see Supplemental Material [35]). The case in Fig. 1(d) is in fact a SOTI.

To achieve this general strategy in real materials, we propose that antidot engineering, constructing regularly spaced holes in the materials [36,37], is a powerful route to induce higher-order topology in 2D Dirac materials. It is a type of experimentally realized functional means in 2D honeycomb-like Dirac materials [38–41]. We theoretically predict the 2D-Xene (X = C, Si, and Ge) antidot lattices (XALs) as an excellent material platform for 2D SOTIs with large band gaps (up to ∼1.78 eV), in which the shape and arrangement of the holes are similar to those of the experimentally designed system [39]; 2D SOTIs in the proposed XALs can be rationalized well not only by nonzero quadrupole polarization [1,2] and the filling anomaly of the OAL [13,14] but also by the 2D generalized Su-Schrieffer-Heeger models {the Kekulé distorted hexagonal lattice (KDHL) model [9]}. The inherent connections between various underlying SOTI mechanisms are established in the XALs. Using first-principles and tight-binding (TB) model calculations along with symmetry analysis, we show a spinless charge fractionalization of $e/2$ at the corner states, protected by the C_6 or $\bar{3}$ [C_3 + inversion(I)] symmetry, as well as weak topological edge states emerging in the XAL band gap. The finite-size effect and the robustness of these corner states against edge perturbations and bulk disorders are explicitly demonstrated. Our results will facilitate the experimental characterization of the SOTI phase in 2D-Xene and suggest that antidot engineering could be a promising strategy to introduce higher-order topology to the 2D Dirac materials.

Results and Discussion. The proposed XAL is simply a triangular array of hexagonal holes in the Xene (X = C, Si, and Ge) sheet, as illustrated in Fig. 2(a). Similar antidot lattices in graphene and silicene have been fabricated in experiments [38–41]. The edge X (X = C, Si, and Ge) atoms of the holes are passivated by hydrogen atoms. Each type of the XAL is denoted by the hole radius R and the wall width W as [R, W]. The R is calculated by $N_{removed} = 6R^2$ (N_{removed} is the number of the removed X atoms in one lattice cell). As an example, Fig. 2(a) shows the [R, W] = [1, 2] graphene antidot lattice (GrAL). The previous work has shown that, only with even W, the patterning of periodic holes of R = 1 can open a substantial band gap around the E_F in the GrAL [42] and silicene antidot lattice (SiAL) [37]. Thus, XALs with R = 1 and W = 2, 4, 6, 8 are discussed in this letter. The GrAL and SiAL/germanene antidot lattice (GeAL) have P6/mmm (No. 191) and P-31m (No. 162) space groups, respectively. The lattice constants of the XALs obtained from the first-principles calculations are nearly unchanged compared with those of the corresponding Xene supercells (see Supplemental Material [35]). The trend is consistent with previous work [34,36,37].

For XALs with R = 1 and even W, the patterning of periodic holes will result in a smaller Brillouin zone (BZ) than that of pristine Xene in such a way that both points K and K' are translated into the origin (Γ point) within the new "folded" BZ. Figure 2(b) shows the example of the first BZs for the 1 × 1 Xene and the [R = 1, W = 2] XAL. The latter has the same first BZ of $\sqrt{12} \times \sqrt{12}$ supercells of Xene.

As shown in Fig. 2(c), one observes a direct band gap of ∼1.78 eV at the Γ point and a twofold degenerate conduction band minimum and valence band maximum forming at the folded Dirac points. Similar band gaps also appear in other GrALs, SiALs, and GeALs in Fig. S1 in the Supplemental Material [35]. The opening of the energy gap in the XALs is mainly due to the mixing of Dirac points at K and K' as well as the intersublattice intervalley scattering [34]. As shown in densities of the states (DOSs) in Fig. 2(c), the low-energy bands of GrAL mainly consist of p_z orbitals that have the same constituents as the Dirac states of the pristine graphene, implying that these come from the Dirac states of the pristine graphene. Similar low-energy band structures can also be found in SiAL and GeAL {Figs. S1(a) and S1(b) in the Supplemental Material [35]}. Since the spin-orbit coupling is very small in the low-energy bands for the XALs [Fig. S1(a) in the Supplemental Material], it is neglected in the calculations and the system can be effectively treated as spinless in the subsequent analysis. Because of the similar electronic structures of these XALs near the E_F, we will focus on the [R = 1, W = 2] GrAL in following.

As displayed in Fig. 2(d), the relatively flat edge state appears in the middle of the band gap of the semi-infinite plane of the GrAL along the armchair edge, which also emerges in the SiAL and the GeAL [Figs. S2(a) and S2(d) in the

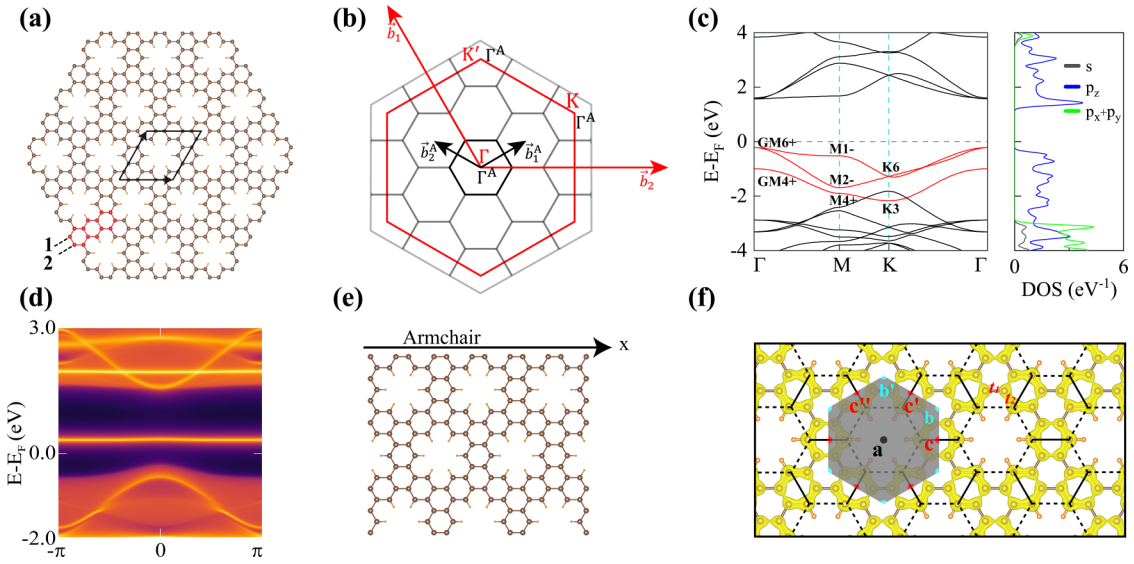

FIG. 2. (a) Crystal structure of the [R = 1, W = 2] GrAL. The brown and orange balls stand for C and H atoms, respectively. (b) BZs. The $\vec{b}_{1,2}$ and $\vec{b}^{A}_{1,2}$ are reciprocal vectors for the 1 × 1 Xene and the [R = 1, W = 2] XAL, respectively. (c) Bulk electronic band structure and DOSs of the [R = 1, W = 2] GrAL. The curves in the left panel correspond to the bands without spin-orbit coupling. (d) The projected spectra for the armchair edge of a semi-infinite sheet of the [R = 1, W = 2] GrAL shown in (e). (e) The semi-infinite sheet of the GrAL with an armchair edge. (f) The total charge densities of the [R = 1, W = 2] GrAL THVBs with an isosurface value of 0.003 $e \cdot$ Å^{-3}. The C_6-symmetric unit cell of the GrAL is illustrated in a gray hexagon and its maximal Wyckoff positions are labeled in black, red, and cyan blue, respectively. The equivalent KDHL model for low low-energy bands of the GrAL is shown in black solid and dotted lines.

Supplemental Material], demonstrating that the XALs are not traditional topological insulators. The topological edge or corner states of a set of occupied bands (without strong or fragile topology) can be understood by analysis of the connectivity of the band representations to find the EBRs, which are a set of subbands induced from placing a certain orbital at a given Wyckoff position [28–32]. We calculated the irreducible representations of the little group at the high-symmetry k points for the occupied bands of the [R = 1, W = 2] GrAL (Table SII in the Supplemental Material [35]) and marked the irreducible representations of the three highest valence bands (THVBs) (plotted in red) in Fig. 2(c), respectively. The results show that the set of the THVBs corresponds to an EBR, whose corresponding localized Wannier centers are at Wyckoff positions of $3c$ ($c - c''$) [red dots in Fig. 2(f)]. The difference between the Wannier function centers of the THVBs and the atomic sites demonstrates that the THVBs are in the OAL [29,30]. Thus the set of bands possess symmetric and localized Wannier functions residing on a different Wyckoff position than the basis orbitals. The origin of the edge states can be attributed to the OAL. Intuitively, if one cuts the GrAL along the line through any of the Wyckoff positions $3c$, exposed Wannier functions will form edge states. For every $k_{\parallel}$ [the k-points in the 1D BZ of the semi-infinite sheet], the corresponding Zak phase of the low-energy bulk bands along the direction perpendicular to the edge is numerically evaluated to be π, dictating the presence of 1D edge states [43], in agreement with the analysis above.

To clearly show the Wannier center of the THVBs, their total charge densities ($\sum_{nk} |\psi_{nk}|^2$, $n \in$ THVBs and $k \in$ BZ) are shown in Fig. 2(f). The charge-density centers, also the Wannier centers of the THVBs, reside on the Wyckoff positions $3c$, consistent with the results above. The charge densities of the THVBs in the GrAL present a regular, approximately planar structure and are very similar to those of the SiAL and GeAL [Fig. S3 in the Supplemental Material]. More interestingly, this type of charge-density distribution can be effectively treated as the hopping amplitudes of a KDHL model, whose planar honeycomb-lattice sites are located on the edge C atoms of the holes, as shown in Fig. 2(f). Due to the different charge-density distributions between the hexagonal sublattices, the effective intracellular hopping (γ, dot line) is distinct from the intercellular hopping (γ', solid line). The previous work has revealed that the KDHL model is in a topological quadrupole phase when $|\gamma| < |\gamma'|$ and can support a flat edge state in the armchair case [5–7], which also emerges in our XALs. Later, we shall see that the low-energy electronic structure of the XAL is equivalent to that in a nontrivial KDHL model [$|\gamma| < |\gamma'|$, the case in Fig. 1(d)].

We now investigate the corner states of the XAL, a hallmark of a 2D SOTI. To illustrate the corner charges, we build open flakes (see Fig. 3 and Figs. S2 and S4) for the XALs. In Fig. 3, we present results for the GrAL flake as a representative of the XAL flakes. The appearance of the corner-localized midgap states indicates the existence of the fractional corner charges in the materials. As displayed in Fig. 3(a), approximately sixfold degenerate states (blue circles) appear around the E_F, whose charge distributions are all localized around the corners of the flake atoms [Fig. 3(b)]. Since only half of the corner states are occupied [Fig. 3(a)], an average spinless corner charge $e/2$ is obtained. The slight energy splitting of the in-gap corner states can be ascribed to the finite size effect [10,11] of the flake built.

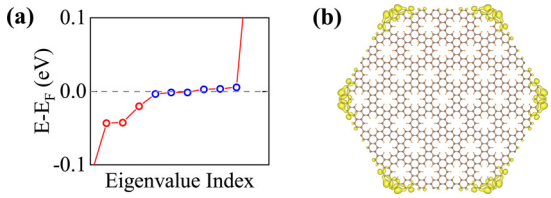

FIG. 3. (a) Discrete energy levels of the hexagonal-shaped [R = 1, W = 2] GrAL flake shown in (b). Six in-gap topological corner states are shown in blue circles. (b) One hexagonal-shaped [R = 1, W = 2] GrAL flake, in which the charge distribution of the six in-gap states is also shown. The isosurface value is set as 0.002 e · Å^{-3}. The charge distributions are localized at the six corners.

The fractional quantization of the corner charge of 2D SOTIs protected by crystal symmetry has been attributed to the mismatched requirements for the number of occupied electrons which need to simultaneously satisfy irreconcilable charge neutrality and the crystal symmetry, named as "filling anomaly" [13,14]. For spinless or spinful OAL with time-reversal symmetry (T), the topological invariants or the symmetry indicators constructed by Benalcazar *et al.* and Schindler *et al.* can be employed to identify the filling anomaly arising from corners [13,14]. As defined in their work, the GrAL belongs to the C_6 group and the SiAL and GeAL belong to the $\bar{3}$ group. For the spinless case, the topological invariants of the C_6 and $\bar{3}$ groups are $\chi^{(6)} = \{[M_1^{(2)}], [K_1^{(3)}]\}$ and $\chi_I^{(3)} = \{[M_-^I], [K_1^{(3)}]\}$, respectively [13]. The invariant $[M_-^I]$, for example, indicates the difference in the number of eigenstates in the occupied bands manifold of the inversion operation (I) indicated by the superscript corresponding to eigenvalue -1 (odd parity) at M and Γ. The obtained $\chi^{(6)} = (2, 0)$ and $\chi_I^{(3)} = (2, 0)$ mean that the GrAL is in the $h_{3c}^{(6)}$ *primitive generator* class, and the SiAL and GeAL correspond to the $h_{3c}^{(\bar{3})}$ primitive generator class [the corresponding Wyckoff positions $3c$ are shown in Fig. 2(f)]. These two primitive generators have the same charge fractionalization and polarization, implying no net dipole in the plane and the corner charge fractionalization with $e/2$ (e) in each $\frac{\pi}{3}$ sector for the spinless (spinful) cases, in agreement with the above DFT results.

In a 2D system with both I and T symmetries, the bulk dipole moment can be determined by checking the parities at time-reversal-invariant momenta (TRIMs) as [7]

$$p_i = \frac{1}{2}\left(\sum_n 2p_i^n \text{modulo} 2\right), \quad p_i^n = \frac{1}{2}q_i^n$$
$$(-1)^{q_i^n} = \frac{\eta^n(M)}{\eta^n(\Gamma)}, \tag{1}$$

where $i = 1$ or 2 denotes the direction of the reciprocal lattice vector, $\eta^n(k)$ is the parity of the nth band at k-point below the E_F, and q_i^n equals either 0 or 1.

The bulk quadrupole moment can be calculated as

$$q_{ij} = \frac{1}{2}\left(\sum_n 2p_i^n p_j^n \text{modulo} 2\right). \tag{2}$$

For the occupied bands of the [R = 1, W = 2] XAL, the obtained bulk dipole and quadrupole moments are $(p_1, p_2) = (0, 0)$ and $q_{12} = \frac{1}{2}$, respectively, the same as the results obtained from the primitive generators above. The corner

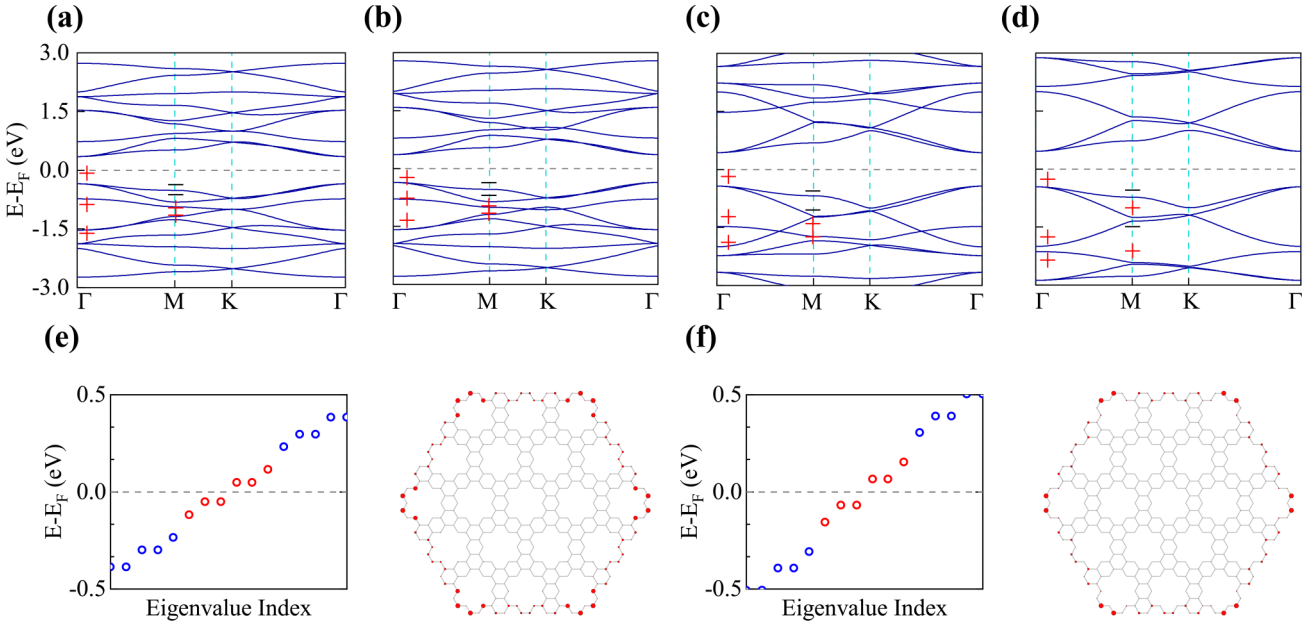

FIG. 4. The band structures calculated from the TB model for a [R = 1, W = 2] XAL with a p_z orbital per X atom site. The hopping parameters for each case are (a) $t_1/t_2 = 1$, (b) $t_1/t_2 = 1.05$, (c) $t_1/t_2 = 1.6$, and (d) $t_1/t_2 = 2.1$. The calculated parities at TRIM are indicated by a red plus sign for even parity and a black minus sign for odd parity. Panels (e) and (f) show low-energy spectra and electronic densities of the six zero-energy states of a finite armchair-terminated [R = 1, W = 2] XAL flake for the cases of (b) and (d), respectively. The six zero-energy states are marked in red in spectra and their electronic densities are marked in red with color scale proportional to the normalized square modulus $|\psi_i|^2$ of the eigenstates.

states of the XAL are therefore caused solely by the quadrupole moment, a topological invariant characterizing the 2D SOTI [1,2].

Note that the results from the total occupied bands of the XAL studied above, for both of the quadrupole moments and the primitive generators, are consistent with the results calculated with only its effective low-energy part (THVBs). Thus, the bulk nontrivial topology is determined solely by the low-energy spectra of the XAL. To deeply understand the low-energy physics of the XAL, a TB Hamiltonian with a p_z orbital per X atom site is constructed as

$$H = t_1 \sum_{\substack{\langle i,\, j\rangle \\ i \text{ or } j \in \text{edge of holes}}} C_i^\dagger C_j + t_2 \sum_{\substack{\langle i,\, j\rangle \\ i,\, j \notin \text{edge of holes}}} C_i^\dagger C_j + \text{H.c.}, \tag{3}$$

where t_1 (t_2) [shown in Fig. 2(f)] denotes the hopping between the edge atoms of the holes (the other atoms) and their nearest neighbors in the XAL, respectively. Considering the difference in the charge densities of the low-energy bands located around the edge atoms of the holes and other atoms in the XAL [Fig. 2(f)], we can distinguish clearly t_1 from t_2. Figures 4(a)–4(d) show the bands calculated by the TB model with $t_1/t_2 = 1$, 1.05, 1.6, and 2.1, respectively. As shown in Figs. 4(a)–4(d), the increase of the t_1/t_2 results in the inversion of the low-energy valence bands around the M and K points. Especially for $t_1/t_2 = 1.05$, the low-energy dispersion features and the parities (and also band representations, not labeled) at the TRIMs [Fig. 4(b)] are the same as those of the GrAL [Fig. 2(c)]. In Fig. 4(c), the fourth valence band moves upward and twists with the second valence band, and it eventually crosses entirely the third valence band with $t_1/t_2 = 2.1$ [Fig. 4(d)]. By checking the connectivity and parities of THVBs, the TB model with $t_1/t_2 = 2.1$ produces similar low-energy bands to those of the nontrivial KDHL model [Fig. 1(d)]. During the band evolution from Fig. 4(a) to Fig. 4(d), the bulk band gap is always open, indicating the bulk topology unchanged and equivalent to that of the nontrivial KDHL model. This equivalence could also be indicated by nonvanishing midgap corner states during the evolution [Figs. 4(e) and 4(f)], which have the identical spatial distribution and quantized fractional charge as the corner states of the nontrivial KDHL model [5,44]. The above analysis of the corner states demonstrates that the low-energy dispersions of XAL, equivalent to the KDHL model, could be comprehended in the OAL and have quantized bulk quadrupole polarization, thus establishing an inherent connection between these three mechanisms.

A set of THVBs of [R = 1, W = 2] XAL supports a disconnected 3D EBR [29] {Bilbao notation [45]: $B_{2g} \uparrow G(3)$ for the GrAL, $A_g \uparrow G(3)$ for the SiAL and GeAL}, which can be decomposed into a 2D representation set and a 1D representation set. This means that the two parts of the THVBs of the XAL can evolve separately below the E_F to keep the bulk topology invariant. The consistency of EBR decomposability for the low-energy bands in the XAL is derived from the common Dirac states and antidot patterns in Xene and this makes the nontrivial bulk topology of the XAL robust against the wall width of the XAL, whose enhancement causes the 1D representation set of the XAL THVBs to evolve away from E_F and toward deeper energies [see Figs. S1(c)–S1(h) in the Supplemental Material].

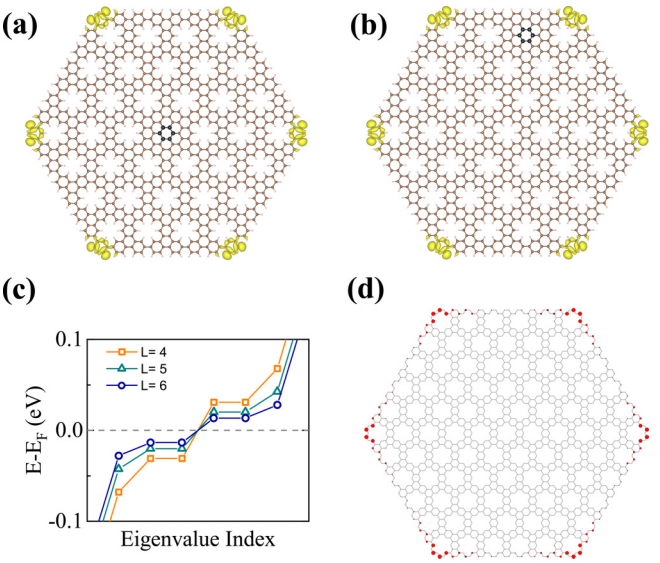

FIG. 5. Panels (a) and (b) show the charge distributions of the six in-gap corner states of the hexagonal-shaped [R = 1, W = 2] GrAL with defects at the center and edge, respectively. The defects are generated by filling one hole in the flakes with six carbon atoms, which are denoted by black color. Panel (c) displays the discrete energy levels for the six corner states of the hexagonal-shaped flakes with varying sizes in the TB models, in which the parameters are fixed at $t_1/t_2 = 1.05$. The flake size, denoted as L, is represented by the number of holes along one edge of the flake. Panel (d) depicts the electronic densities of the six corner states of the $L = 6$ flake, which is proportional to the normalized square modulus $|\psi_i|^2$ of the eigenstates.

As shown in Fig. S4 in the Supplemental Material, we calculate the corner states for several GrAL and SiAL flakes with various sizes, wall width, and edge shape. All the flakes have nontrivial corner states, indicating the robustness of the XAL corner states.

To further test the robustness of the XAL corner states against bulk disorder, we constructed two flakes with defects at the center and edge, respectively. As shown in Figs. 5(a) and 5(b), the bulk disorders have no influence on the charge distributions of the corner states, which demonstrates the robustness of the XAL corner states against low-density bulk disorders. To validate the finite-size effect of the topological corner states, we built three different sizes of flakes for the TB model, the results of which are plotted in Figs. 5(c) and 5(d). As the flake size increases (from $L = 4$ to $L = 6$), the energy splitting of the in-gap topological corner states becomes smaller and smaller, while the charge distribution of corner states remains consistent, which clearly exhibits the finite-size effect.

In summary, we show that antidot engineering is an effective means of implementing the large band-gap SOTI in 2D Xene. The bulk quadrupole moment, the primitive generators, and the TB model yield identical results for the spatial distribution and the quantized fractional charge of corner states in the XAL, respectively. This consistency demonstrates an

inherent relevance of the higher-order topological mechanisms of the nonzero quadrupole polarization, the filling anomaly, and the 2D generalized Su-Schrieffer-Heeger model. These results demonstrate the feasibility of the universal proposal for realizing SOTIs in 2D Dirac materials by introducing symmetry-preserving perturbations that extend the unit cell. Our work creates an experimentally accessible path to design novel SOTIs with robust corner states.

Acknowledgments. This work was supported by National Natural Science Foundation of China under No. 11904101, No. 11874117, and No. 11604134 and the Natural Science Foundation of Shanghai under No. 21ZR1408200.

[1] W. A. Benalcazar, B. A. Bernevig, and T. L. Hughes, Quantized electric multipole insulators, Science **357**, 61 (2017).

[2] W. A. Benalcazar, B. A. Bernevig, and T. L. Hughes, Electric multipole moments, topological multipole moment pumping, and chiral hinge states in crystalline insulators, Phys. Rev. B **96**, 245115 (2017).

[3] Z. Song, Z. Fang, and C. Fang, (d-2)-Dimensional Edge States of Rotation Symmetry Protected Topological States, Phys. Rev. Lett. **119**, 246402 (2017).

[4] F. Schindler, A. M. Cook, M. G. Vergniory, Z. Wang, S. S. Parkin, B. A. Bernevig, and T. Neupert, Higher-order topological insulators, Sci. Adv. **4**, eaat0346 (2018).

[5] T. Mizoguchi, H. Araki, and Y. Hatsugai, Higher-order topological phase in a honeycomb-lattice model with anti-kekulé distortion, J. Phys. Soc. Jpn. **88**, 104703 (2019).

[6] F. Liu, M. Yamamoto, and K. Wakabayashi, Topological edge states of honeycomb lattices with zero berry curvature, J. Phys. Soc. Jpn. **86**, 123707 (2017).

[7] F. Liu, H.-Y. Deng, and K. Wakabayashi, Helical Topological Edge States in a Quadrupole Phase, Phys. Rev. Lett. **122**, 086804 (2019).

[8] J. Langbehn, Y. Peng, L. Trifunovic, F. von Oppen, and P. W. Brouwer, Reflection-Symmetric Second-Order Topological Insulators and Superconductors, Phys. Rev. Lett. **119**, 246401 (2017).

[9] S. K. Radha and W. R. L. Lambrecht, Buckled honeycomb antimony: Higher order topological insulator and its relation to the kekulé lattice, Phys. Rev. B **102**, 115104 (2020).

[10] X.-L. Sheng, C. Chen, H. Liu, Z. Chen, Z.-M. Yu, Y. X. Zhao, and S. A. Yang, Two-Dimensional Second-Order Topological Insulator in Graphdiyne, Phys. Rev. Lett. **123**, 256402 (2019).

[11] B. Liu, G. Zhao, Z. Liu, and Z. Wang, Two-dimensional quadrupole topological insulator in γ-graphyne, Nano Lett. **19**, 6492 (2019).

[12] M. J. Park, Y. Kim, G. Y. Cho, and S. B. Lee, Higher-Order Topological Insulator in Twisted Bilayer Graphene, Phys. Rev. Lett. **123**, 216803 (2019).

[13] W. A. Benalcazar, T. Li, and T. L. Hughes, Quantization of fractional corner charge in c_n-symmetric higher-order topological crystalline insulators, Phys. Rev. B **99**, 245151 (2019).

[14] F. Schindler, M. Brzezińska, W. A. Benalcazar, M. Iraola, A. Bouhon, S. S. Tsirkin, M. G. Vergniory, and T. Neupert, Fractional corner charges in spin-orbit coupled crystals, Phys. Rev. Research **1**, 033074 (2019).

[15] B. Xie, H.-X. Wang, X. Zhang, P. Zhan, J.-H. Jiang, M. Lu, and Y. Chen, Higher-order band topology, Nat. Rev. Phys. **3**, 520 (2021).

[16] M. Ezawa, Higher-Order Topological Insulators and Semimetals on the Breathing Kagome and Pyrochlore Lattices, Phys. Rev. Lett. **120**, 026801 (2018).

[17] F. K. Kunst, G. van Miert, and E. J. Bergholtz, Lattice models with exactly solvable topological hinge and corner states, Phys. Rev. B **97**, 241405(R) (2018).

[18] Y. Xu, R. Xue, and S. Wan, Topological corner states on kagome lattice based chiral higher-order topological insulator, arXiv:1711.09202.

[19] A. Molle, J. Goldberger, M. Houssa, Y. Xu, S.-C. Zhang, and D. Akinwande, Buckled two-dimensional xene sheets, Nat. Mater. **16**, 163 (2017).

[20] J. Wang, S. Deng, Z. Liu, and Z. Liu, The rare two-dimensional materials with dirac cones, Natl. Sci. Rev. **2**, 22 (2015).

[21] M. Wu, Z. Wang, J. Liu, W. Li, H. Fu, L. Sun, X. Liu, M. Pan, H. Weng, and M. Dincă, Conetronics in 2d metal-organic frameworks: double/half dirac cones and quantum anomalous hall effect, 2D Mater. **4**, 015015 (2016).

[22] K. S. Novoselov, A. K. Geim, S. V. Morozov, D. Jiang, Y. Zhang, S. V. Dubonos, I. V. Grigorieva, and A. A. Firsov, Electric field effect in atomically thin carbon films, Science **306**, 666 (2004).

[23] B. Feng, Z. Ding, S. Meng, Y. Yao, X. He, P. Cheng, L. Chen, and K. Wu, Evidence of silicene in honeycomb structures of silicon on ag (111), Nano Lett. **12**, 3507 (2012).

[24] M. Dávila, L. Xian, S. Cahangirov, A. Rubio, and G. Le Lay, Germanene: A novel two-dimensional germanium allotrope akin to graphene and silicene, New J. Phys. **16**, 095002 (2014).

[25] Z. Ni, Q. Liu, K. Tang, J. Zheng, J. Zhou, R. Qin, Z. Gao, D. Yu, and J. Lu, Tunable bandgap in silicene and germanene, Nano Lett. **12**, 113 (2012).

[26] C. L. Kane and E. J. Mele, Quantum Spin Hall Effect in Graphene, Phys. Rev. Lett. **95**, 226801 (2005).

[27] C.-C. Liu, W. Feng, and Y. Yao, Quantum Spin Hall Effect in Silicene and Two-Dimensional Germanium, Phys. Rev. Lett. **107**, 076802 (2011).

[28] J. Zak, Band representations and symmetry types of bands in solids, Phys. Rev. B **23**, 2824 (1981).

[29] B. Bradlyn, L. Elcoro, J. Cano, M. Vergniory, Z. Wang, C. Felser, M. Aroyo, and B. A. Bernevig, Topological quantum chemistry, Nature (London) **547**, 298 (2017).

[30] J. Cano, B. Bradlyn, Z. Wang, L. Elcoro, M. G. Vergniory, C. Felser, M. I. Aroyo, and B. A. Bernevig, Building blocks of topological quantum chemistry: Elementary band representations, Phys. Rev. B **97**, 035139 (2018).

[31] R.-J. Slager, A. Mesaros, V. Juričić, and J. Zaanen, The space group classification of topological band-insulators, Nat. Phys. **9**, 98 (2013).

[32] J. Kruthoff, J. De Boer, J. Van Wezel, C. L. Kane, and R.-J. Slager, Topological Classification of Crystalline Insulators Through Band Structure Combinatorics, Phys. Rev. X **7**, 041069 (2017).

[33] B. Bradlyn, Z. Wang, J. Cano, and B. A. Bernevig, Disconnected elementary band representations, fragile topology, and wilson loops as topological indices: An example on the triangular lattice, Phys. Rev. B **99**, 045140 (2019).

[34] J.-S. Park and H. J. Choi, Band-gap opening in graphene: A reverse-engineering approach, Phys. Rev. B **92**, 045402 (2015).

[35] See Supplemental Material at http://link.aps.org/supplemental/10.1103/PhysRevResearch.3.L042044 for calculation methods, band representations of GrALs, energy bands, edge and corner states of SiALs and GeALs.

[36] T. G. Pedersen, C. Flindt, J. Pedersen, N. A. Mortensen, A.-P. Jauho, and K. Pedersen, Graphene Antidot Lattices: Designed Defects and Spin Qubits, Phys. Rev. Lett. **100**, 136804 (2008).

[37] F. Pan, Y. Wang, K. Jiang, Z. Ni, J. Ma, J. Zheng, R. Quhe, J. Shi, C. Chen, and J. Lu, Silicene nanomesh, Sci. Rep. **5**, 9075 (2015).

[38] J. Bai, X. Zhong, S. Jiang, Y. Huang, and X. Duan, Graphene nanomesh, Nat. Nanotechnol. **5**, 190 (2010).

[39] J. Mahmood, E. K. Lee, M. Jung, D. Shin, I.-Y. Jeon, S.-M. Jung, H.-J. Choi, J.-M. Seo, S.-Y. Bae, S.-D. Sohn, N. Park, J. H. Oh, H.-J. Shin, and J.-B. Baek, Nitrogenated holey two-dimensional structures, Nat. Commun. **6**, 6486 (2015).

[40] L. Meng, Y. Wang, L. Zhang, S. Du, R. Wu, L. Li, Y. Zhang, G. Li, H. Zhou, and W. A. Hofer, Buckled silicene formation on ir (111), Nano Lett. **13**, 685 (2013).

[41] M. Kim, N. S. Safron, E. Han, M. S. Arnold, and P. Gopalan, Fabrication and characterization of large-area, semiconducting nanoperforated graphene materials, Nano Lett. **10**, 1125 (2010).

[42] F. Ouyang, S. Peng, Z. Liu, and Z. Liu, Bandgap opening in graphene antidot lattices: the missing half, ACS Nano **5**, 4023 (2011).

[43] P. Delplace, D. Ullmo, and G. Montambaux, Zak phase and the existence of edge states in graphene, Phys. Rev. B **84**, 195452 (2011).

[44] C.-Y. Hou, C. Chamon, and C. Mudry, Electron Fractionalization in Two-Dimensional Graphenelike Structures, Phys. Rev. Lett. **98**, 186809 (2007).

[45] M. I. Aroyo, A. Kirov, C. Capillas, J. Perez-Mato, and H. Wondratschek, Bilbao crystallographic server. ii. Representations of crystallographic point groups and space groups, Acta Crystallogr. Sect. Ay **62**, 115 (2006).